

Rapid Intraoperative Diagnosis of Pediatric Brain Tumors Using Stimulated Raman Histology

Todd C. Hollon¹, Spencer Lewis², Balaji Pandian², Yashar S. Niknafs², Mia R. Garrard¹, Hugh Garton¹, Cormac O. Maher¹, Kathryn McFadden³, Matija Snuderl⁴, Andrew P. Lieberman³, Karin Muraszko¹, Sandra Camelo-Piragua³, and Daniel A. Orringer¹



Abstract

Accurate histopathologic diagnosis is essential for providing optimal surgical management of pediatric brain tumors. Current methods for intraoperative histology are time- and labor-intensive and often introduce artifact that limit interpretation. Stimulated Raman histology (SRH) is a novel label-free imaging technique that provides intraoperative histologic images of fresh, unprocessed surgical specimens. Here we evaluate the capacity of SRH for use in the intraoperative diagnosis of pediatric type brain tumors. SRH revealed key diagnostic features in fresh tissue specimens collected from 33 prospectively enrolled pediatric type brain tumor patients, preserving tumor cytology and histoarchitecture in all specimens. We simulated an intraoperative consultation for 25 patients with specimens imaged using both SRH and standard hematoxylin and eosin histology. SRH-based diagnoses achieved near-perfect diagnostic concordance (Cohen's kappa, $\kappa >$

0.90) and an accuracy of 92% to 96%. We then developed a quantitative histologic method using SRH images based on rapid image feature extraction. Nuclear density, tumor-associated macrophage infiltration, and nuclear morphology parameters from 3337 SRH fields of view were used to develop and validate a decision-tree machine-learning model. Using SRH image features, our model correctly classified 25 fresh pediatric type surgical specimens into normal versus lesional tissue and low-grade versus high-grade tumors with 100% accuracy. Our results provide insight into how SRH can deliver rapid diagnostic histologic data that could inform the surgical management of pediatric brain tumors.

Significance: A new imaging method simplifies diagnosis and informs decision making during pediatric brain tumor surgery. *Cancer Res*; 78(1); 278–89. ©2017 AACR.

Introduction

Accurate histopathologic diagnosis is essential for providing optimal surgical management of pediatric brain tumors. Intraoperative decision-making and surgical goals diverge depending on tumor pathology. The current standard of care for intraoperative diagnosis includes frozen sectioning and cytologic preparations performed by skilled technicians and pathologists working in dedicated surgical pathology laboratories with complex infrastructure (1). The current time- and labor-intensive workflow of intraoperative pathology results may delay diagnosis and surgical care. Moreover, current histologic methods may introduce artifact that limits interpretation if additional tissue is not provided. Furthermore, cryostat preparation consumes tissue that may be essential for arriving at a final diagnosis.

¹Department of Neurosurgery, University of Michigan, Ann Arbor, Michigan.

²School of Medicine, University of Michigan, Ann Arbor, Michigan. ³Department of Pathology, University of Michigan, Ann Arbor, Michigan. ⁴Department of Pathology, New York University Langone Medical Center, New York, New York.

Note: Supplementary data for this article are available at Cancer Research Online (<http://cancerres.aacrjournals.org/>).

S. Camelo-Piragua and D.A. Orringer are co-corresponding author.

Corresponding Authors: Daniel A. Orringer, University of Michigan, 1500 E. Medical Center Dr., 3552 Taubman Ctr, Ann Arbor, MI 48109. Phone: 734-615-4638; E-mail: dorringer@med.umich.edu; and Sandra Camelo-Piragua, sandraca@med.umich.edu

doi: 10.1158/0008-5472.CAN-17-1974

©2017 American Association for Cancer Research.

Alternatives to standard hematoxylin and eosin (H&E) histology for intraoperative pathology have been proposed (2–4) but have yet to be adopted given their limitations. An ideal method for intraoperative histology would rapidly deliver diagnostic histologic images within a streamlined workflow requiring minimal tissue preparation. Such an imaging system would enable (i) prompt and accurate histopathologic diagnosis and (ii) serial specimen processing for detection of residual tumor burden. With residual tumor burden being a major modifiable risk factor in common pediatric brain tumors (5–9), evaluation of tissue within the resection cavity could allow for greater extent of resection and improve overall survival.

Stimulated Raman scattering (SRS) microscopy creates the possibility of rapid, label-free, high-resolution microscopic imaging of unprocessed surgical tissues (10–12). SRS microscopy yields histologic images using the intrinsic vibrational properties of biological macromolecules, such as lipids, proteins, and DNA. Clinical SRS microscopy relying on fiber-laser technology and a virtual H&E color scheme, called stimulated Raman histology (SRH), has recently been shown to provide histopathologic images comparable to conventional histology in a series of neurosurgical specimens (13). Previous investigations were proof-of-concept studies that focused on the feasibility of using machine-learning techniques for SRH-based diagnosis in the adult population. These previous machine-learning classification methods were tailored for adult brain tumor pathologies and lacked sufficiently model interpretability to translate to pediatric brain tumors. Brain tumors that predominate in the pediatric population, such as pilocytic astrocytomas, ependymomas, and

embryonal tumors, have unique histologic features that represent a distinct diagnostic challenge both for neuropathologists and computer aided-diagnostic strategies. Moreover, differentiating between low-grade and high-grade tumors (e.g., ependymomas, WHO grade II, vs. medulloblastomas, WHO grade IV) has a major impact on decision-making during surgery and is essential for establishing optimal surgical management (5–9). To date, the potential for SRH to impact the surgical care of pediatric patients has not been rigorously evaluated.

Here, we evaluate the ability of SRH to provide rapid and diagnostic histologic images for pediatric type brain tumors. We demonstrate that SRS microscopy is indeed an effective system for intraoperative histology and eliminates freezing artifact, sectioning, and staining. Accurate diagnosis of pediatric brain tumors is facilitated through SRH as it preserves both cytologic and histomorphological features of fresh tumor specimens. We report a novel quantitative image-processing method that extracts key histopathologic features in neoplastic tissues capable of assisting rapid detection of residual tumor burden and tumor grading based on SRH image feature extraction. Quantitative feature attributes from SRH images were then used to develop and validate a machine-learning model to deliver rapid, automated classification of neoplastic tissue and tumor grade, thereby assisting tumor resection and establishing optimal surgical goals. In summary, our data indicate that SRH holds promise for improving the surgical care of pediatric type brain tumors.

Patients and Methods

Study design

The study was approved by the University of Michigan Institutional Review Board (HUM00083059). Patient studies were conducted in accordance with the Declaration of Helsinki, International Ethical Guidelines for Biomedical Research Involving Human Subjects (CIOMS), Belmont Report and U.S. Common Rule. Patients were prospectively enrolled for 24 months with the following inclusion criteria: (i) male and female subjects undergoing brain tumor resection at the University of Michigan Health System, (ii) subject or medical decision maker was able to provide informed written consent and (iii) subjects in whom there was excess tumor tissue beyond what was needed for routine diagnosis. All patients 18 years or younger were included in the study preoperatively. Patients older than 18 years were enrolled postoperatively if they were diagnosed with pediatric type pathologies to increase study enrollment and ensure a patient cohort of representative pediatric type histology, including pilocytic astrocytoma, ependymoma, medulloblastoma and other embryonal tumors, ganglioglioma, diffuse midline glioma, hemangioblastoma, choroid plexus papilloma, chordoma, and germinoma. The list of pediatric type pathologies was provided by our expert panel of neuropathologists (S. Camelo-Piragua, A.P. Lieberman, K.A. McFadden). Normal/non-neoplastic specimens were taken from a cohort of adult epilepsy and brain tumor patients. The primary goals of the investigation were to (i) establish SRH as a feasible method for obtaining histopathologic diagnosis in tumors common in the pediatric population and (ii) develop a machine-learning method using quantitative SRH image features to provide rapid, automated detection of lesional tissue and tumor grade. Patients were recruited consecutively at a high-volume, tertiary-care hospital to obtain a representative sample of pediatric type brain tumors. All collected specimens

were imaged immediately after removal with our clinical fiber-laser-based SRS microscope (13). A board-certified neuropathologist (A.P. Lieberman) reviewed all images from both standard intraoperative pathology and SRH to determine adequacy and classify each specimen following the current World Health Organization (WHO) diagnostic classification criteria (14). We then implemented a web-based survey with three neuropathologists (S. Camelo-Piragua, K.A. McFadden, M. Snuderl) to determine the diagnostic concordance and accuracy of SRH compared to standard intraoperative H&E histology. To develop a quantitative histology, we used CellProfiler for image feature extraction (15). Image features were then used to develop and validate a random forest machine-learning method to provide automated classification of lesional tissue (i.e., normal vs. lesional) and tumor grade (i.e., low grade vs. high grade).

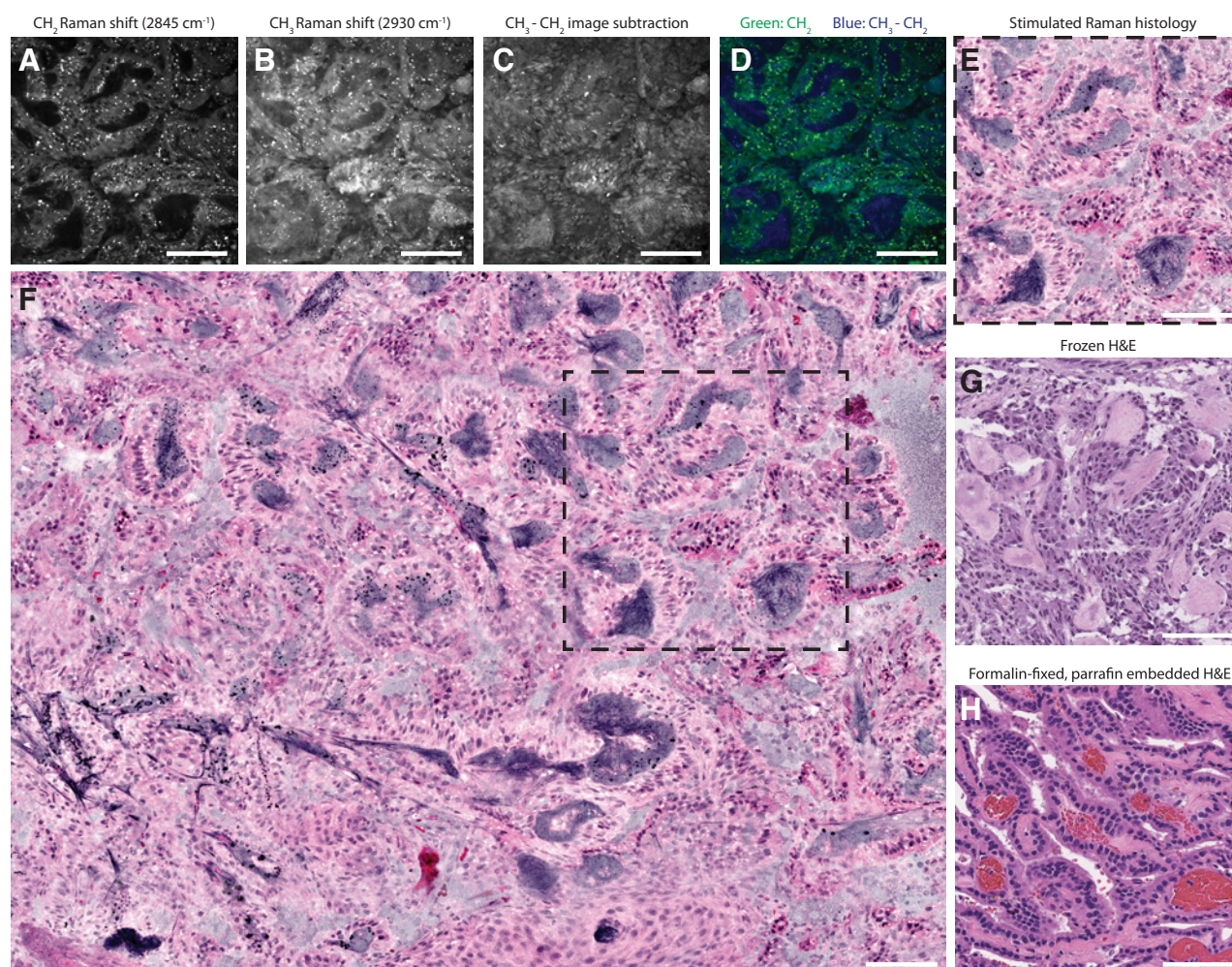
Tissue collection and intraoperative SRH

Following standard operative procedures, neurosurgeons (D.A. Orringer, C.O. Maher, H.J.L. Garton, K.M. Muraszko) removed lesional tissue. Specimens were then split by the neurosurgeon with equal halves sent for intraoperative pathology and for SRH. Standard intraoperative pathology included cytologic preparation and frozen sectioning. To image fresh surgical specimens using the clinical SRS microscope, a small (approximately, $3 \times 3 \times 3$ mm or 27 μ L) unprocessed and unlabeled specimen was placed on a standard uncoated glass slide covered with a cover slip. Using custom imaging programs in μ -Manager and ImageJ software, 400×400 - μ m images from two SRS channels, 2845 cm^{-1} (CH_2/lipid channel) and 2930 cm^{-1} ($\text{CH}_3/\text{protein}$ channel) Raman shift wavenumbers, were obtained in a raster fashion. A mosaic image with automated image stitching was completed to obtain wider fields of view (FOV). In addition to $2,845$ and $2,930\text{ cm}^{-1}$ channel grayscale images, virtual H&E color scheme was used for histopathologic diagnosis (Fig. 1; ref. 13).

Survey methodology

The web-based survey consisted of 25 cases, including 20 pediatric type brain tumors and 5 normal specimens from epilepsy operations. The survey was given to three blinded neuropathologists (S. Camelo-Piragua, K.A. McFadden, M. Snuderl). All cases included both SRH and conventional H&E histology (frozen sections and cytologic preparations), which were admixed and presented in random order. To simulate an intraoperative consultation, a short clinical narrative that included age group, sex, presenting symptoms, and tumor location accompanied each image. Responses were then scored for concordance and accuracy on the following three levels: (i) lesional versus nonlesional tissue for all specimens, (ii) high-grade versus low-grade pathology for tumor specimens, and (iii) diagnostic interpretation for all specimens. The clinical intraoperative pathologic diagnosis provided at the time of surgery was considered the "ground truth." Final WHO classification diagnoses using permanent sections were also recorded to document any discrepancies between intraoperative and final pathologic diagnosis; none were identified upon the review of our supervising neuropathologist (A.P. Lieberman). Diagnostic concordance was determined based on equivalent survey responses for H&E pathology and SRH images (survey-to-survey comparison). Diagnostic accuracy was determined by comparing the survey responses to the University of Michigan Health System diagnosis (survey-to-truth comparison).

Hollon et al.

**Figure 1.**

Label-free SRH of fresh brain tumor tissue. A choroid plexus papilloma, WHO grade I, imaged at 2,845 cm⁻¹ (A) and 2,930 cm⁻¹ (B) Raman shift wavenumbers with 400 × 400-μm FOV at a rate of 2 seconds per frame. C, To highlight nuclear contrast, 2,930 cm⁻¹ image was subtracted from the 2,845 cm⁻¹ image in a single post-processing. D, Two-channel blue-green image was generated by assigning blue gradient to the 2,930 to 2,845 cm⁻¹ pixel intensity and green to the 2,845 cm⁻¹ pixel intensity. Our H&E color lookup table was applied to produce SRH (E) to emulate standard H&E staining of frozen (G) and formalin-fixed, paraffin-embedded (H) sections. F, SRH mosaics were created by automated stitching of individual SRH tiles (dashed square). Scale bars, 100 μm.

Digital image processing of SRH images for quantitative histology

To extract histologic features from SRH images, we used CellProfiler, an automated image analysis application for measuring cellular phenotypes in biological images (15). Three main histologic features were used for digital image analysis: (i) nuclear density, (ii) tumor-associated macrophage (TAM) density, and (iii) nuclear morphology. These image features were selected because they represent known histopathologic changes that occur in neoplastic tissues and because SRH is amenable to extracting these image features. A CellProfiler pipeline was developed using the two SRS image channels for parallel processing of both tumor/normal cell nuclei (2,930–2,845 cm⁻¹ subtracted image) and TAM (2,845 cm⁻¹ image) segmentation. To glean information about nuclear anaplasia, a feature of neoplastic, aberrant differentiation, and growth, we used 11 nuclear morphology parameters (area, perimeter, eccentricity, minimum feret diameter,

maximum feret diameter, compactness, solidity, form factor, extent, orientation, maximum radius) to quantify the shape and size of segmented nuclei. Features were extracted from each 400 × 400-μm SRH FOV. Nuclear and TAM density were calculated as raw counts for each FOV. Nuclear morphology measures were calculated for each segmented cell, and then averaged over each field of view for further analysis. A detailed description of our CellProfiler pipeline modules can be found in Supplementary Table S1.

Machine-learning model for automated histopathologic classification

A random forest model was used to conduct decision tree-based supervised machine learning on SRH image features in order to rapidly identify residual tumor and malignant tissue (16). A random forest machine-learning technique was chosen for model performance and interpretability. Random forest model was built

and validated using R version 3.3.1. Package "randomForest" was used for rapid implementation of random forest and recursive partitioning algorithms. Model training and cross-validation was conducted using the "caret" package. Out-of-bag accuracy was used for model optimization and to select the highest performing mtry hyperparameter. Number of trees to grow was set at 500. Node impurity was measured by the Gini index.

Twenty-five SRH mosaic images/specimens were selected by our supervising neuropathologist (A.P. Lieberman) to be included for the development and validation of two random forest models: Model (i) differentiates normal versus lesional tissue and model (ii) differentiates low-grade versus high-grade tissue. Image tiles within a mosaic that did not contain tissue were excluded. The same extracted image feature data were used for both random forest models as described above. Because of restricted sample size, model evaluation was achieved using 10-fold cross-validation completed independently for each model. Each model's performance was evaluated on two levels: (i) SRH FOV/tile ($400 \times 400\text{-}\mu\text{m}$) level and (ii) SRH mosaic level. Model 1 contained 1,780 SRH FOVs and model 2 contained 1,557 SRH FOVs. Because model predictions occurred at the SRH FOV level, we implemented a FOV-based modal approach to scale the model predictions to the mosaic level. The most common, or modal, predicted FOV class was assigned to the mosaic as a whole. A modal-predicted approach allows for the most represented histopathology within an SRH mosaic to provide the mosaic-level classification.

Statistical analysis

For each pathologist, we calculated Cohen's kappa statistic for normal versus lesional, low-grade versus high-grade, and diagnostic class to determine concordance between SRH and H&E histology (17). This analysis provides information on how well SRH and H&E agree. Cohen's kappa was also calculated for SRH versus truth and for H&E versus truth. This analysis provides information on how well each pathologist was able to detect the truth from SRH and H&E histology (intrarater accuracy). Seven diagnostic classes were included for analysis: embryonal tumors (6), normal/non-neoplastic (5), pilocytic astrocytoma (5), circumscribed glioma/glioneuronal tumor (4, including ganglioglioma, pleomorphic xanthoastrocytoma, and angiocentric glioma), ependymoma (2), other (2, including germinoma and hemangioblastoma), and diffuse midline glioma (1). Finally, we calculated the reliability among the three pathologists using Fleiss' kappa statistic (interrater accuracy) (18).

For comparing the quantitative image features between normal tissue, low-grade tumors, and high-grade tumors, ANOVA testing was used to compare feature means. All statistical comparisons were made using an alpha of 0.05. ROC curves were generated and area under the curve (AUC) was calculated for random forest classifier using "pROC" and "ggplot2" packages. The R Environment of Statistical Computing (version 3.3.1; <http://www.r-project.org>) was used for all statistical analyses.

Results

SRH reveals diagnostic features of pediatric brain tumors

SRH images from 33 patients were reviewed for histopathologic features that would allow for classification of pediatric type brain tumors (see Supplementary Table S2 for patient list). Histologic features of normal brain specimens were demonstrated in SRH

images. Large pyramidal cell bodies of neurons were visualized in neocortex (Fig. 2) of epilepsy patients. SRH highlights lipofuscin pigment within the neuronal body as bright red signaling. Unlike conventional H&E histology, axons are well visualized (Fig. 2). Subcortical white matter shows distinct histologic features compared to neocortex, with dense regions of myelinated axons and interspersed oligodendrocytes (Fig. 2). Fresh cadaveric brain tissue from the striatum (caudate) demonstrates neuronal cell bodies in deep gray matter admixed with white matter tracts (Fig. 2).

Low-grade pediatric brain tumors showed distinct histopathologic features compared to normal brain tissue. Pilocytic astrocytoma, WHO grade I, has distinctive hair-like (piloid) processes (Fig. 2). Ganglioglioma shows large neoplastic ganglion-like cells with occasional bi-nucleation and a mixed glial neoplastic component (Fig. 2). Unlike conventional H&E, the presence of naked axons (white lines) on SRH provides additional helpful information to easily differentiate infiltrative versus well-circumscribed tumors. Pleomorphic xanthoastrocytoma, WHO grade II, shows pleomorphic large tumor cells and giant lipidized glial tumor cells (Fig. 2).

Distinctive features are also seen on SRH in high-grade tumors. Diffuse midline glioma, WHO grade IV, shows areas of anaplasia and microvascular proliferation (Fig. 2). Medulloblastoma and other embryonal tumors, WHO grade IV, demonstrate small round blue cell morphology and marked hypercellularity (Fig. 2). SRH revealed a subpopulation of TAMs in high-grade pediatric tumors. Phagocytosed cellular debris results in high intracellular lipid content and resulting high $2,845\text{ cm}^{-1}$ signal from the cytoplasm of TAMs.

SRH reveals diagnostic cytoarchitectural features and differentiates tumors of posterior fossa

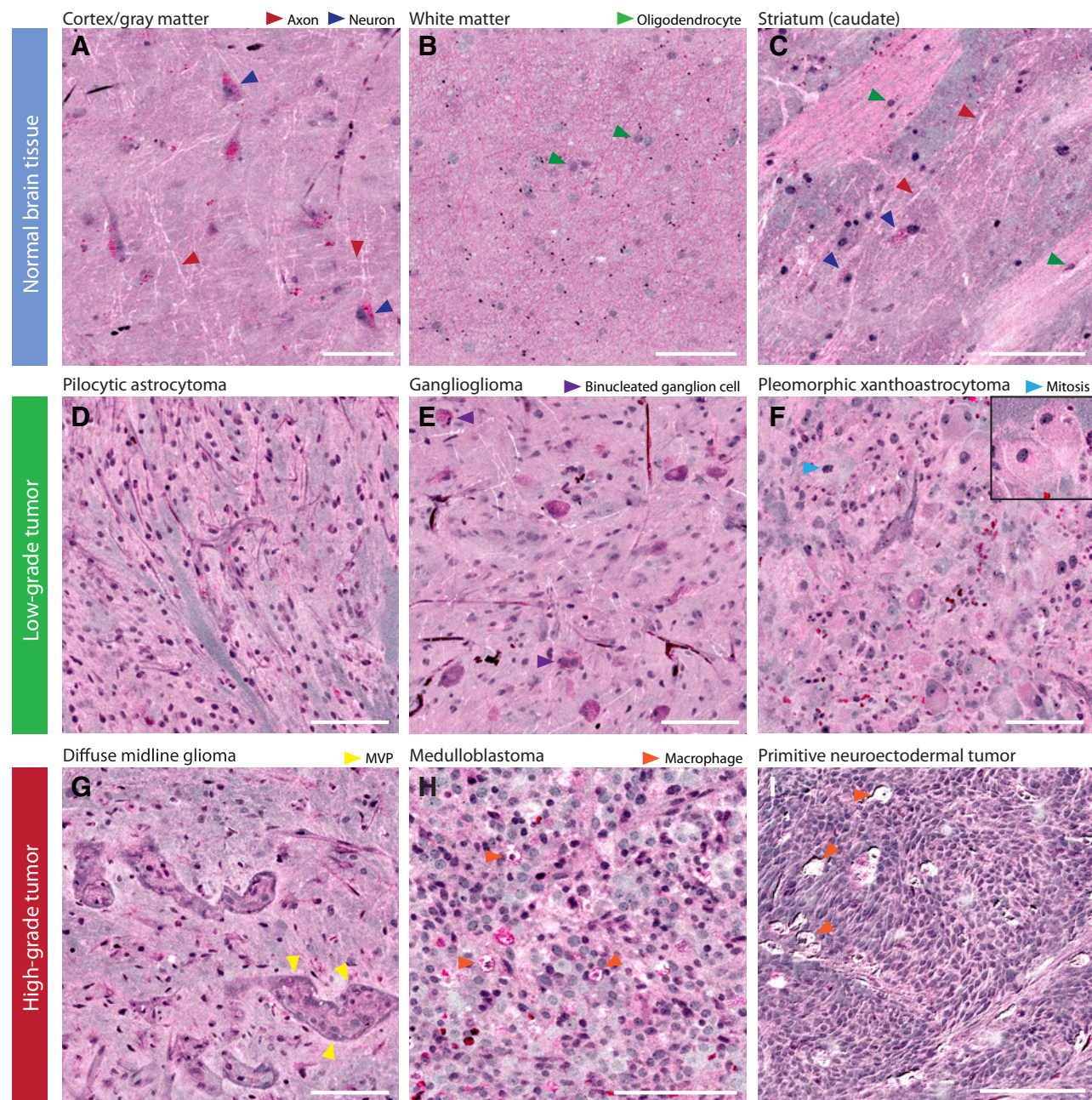
Differentiating the most common pediatric tumors of the posterior fossa is essential due to divergent surgical goals depending on intraoperative diagnosis. Pilocytic astrocytomas, WHO grade I, shown in Fig. 3, have regions of dense tumor with high cellularity mixed with pauci-cellular microcystic regions (biphasic pattern). Rosenthal fibers, dense consolidations of glial fibrillary acidic protein commonly seen in pilocytic astrocytomas, are visualized as black on SRH due to an intense $2,930\text{ cm}^{-1}$ SRS signal. Ependymomas, WHO grade I, show rosette and perivascular pseudorosette formation, both distinctive histoarchitectural structures captured by SRH. Medulloblastomas have primitive cellular morphology, round and angulated nuclei, and Homer-Wright rosette formation (Fig. 3).

Because SRH is a label-free imaging method of fresh, unprocessed surgical specimens, tissue processing artifacts seen with cytologic preparations or frozen sectioning are avoided. Fig. 4 shows a germinoma with preserved cytologic and histoarchitectural features. Large tumor cells with prominent nucleoli represent the major cell population. A second population of mature, non-neoplastic perivascular lymphocytes is also well visualized. The corresponding intraoperative H&E pathology, including smear preparation and frozen H&E section, demonstrates loss of histoarchitectural features and extensive freezing artifact that limits interpretation.

Simulated intraoperative pathology consultation

Having demonstrated that histologic features of normal brain tissue and common pediatric brain tumors are present in SRH

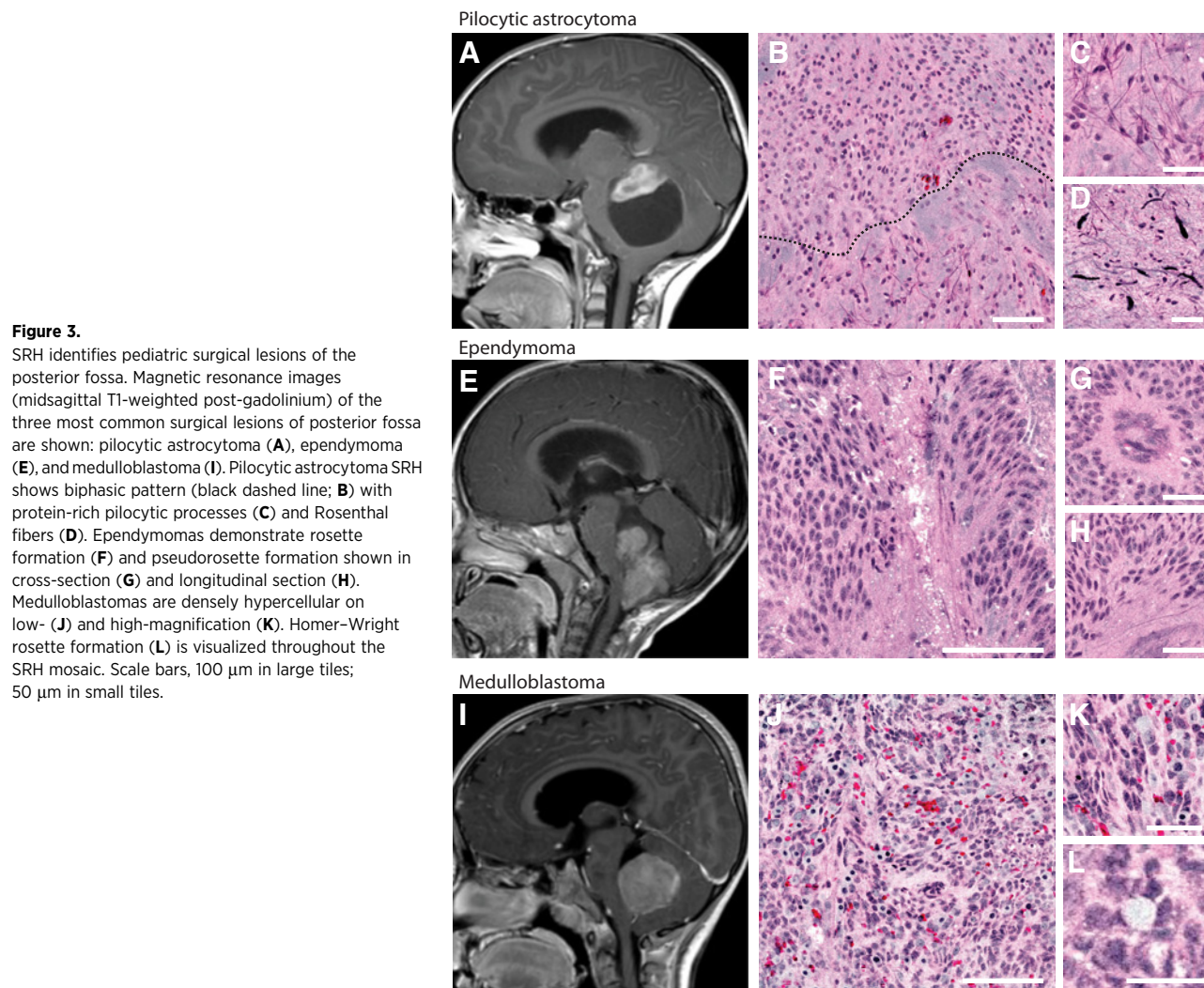
Hollon et al.

**Figure 2.**

SRH histopathologic features of normal brain and pediatric brain tumors. **A**, Normal neocortex shows large pyramidal neurons with lipofuscin cytoplasmic inclusions seen in bright pink. Axons are clearly visualized in neocortex as white lines. **B**, Normal subcortical white matter shows oligodendrocytes embedded in a background of pink, bulbous densely myelinated axons. **C**, Striatum from a cadaveric specimen shows deep gray matter neurons with striated white matter tracts. **D**, Pilocytic astrocytoma shows long, delicate piloid glial processes. **E**, Ganglioglioma has large binucleated ganglion cells in a glial background. **F**, Pleomorphic xanthoastrocytoma with massive lipidized tumor cells (inset). **G**, Diffuse midline glioma show microvascular proliferation and anaplasia. **H** and **I**, Medulloblastoma (**H**) and other embryonal tumors (**I**) show hypercellular, small round blue cell morphology and TAM infiltration. Scale bars, 100 μ m. (MVP, microvascular proliferation).

images, we aimed to quantify the ability of SRH to deliver images for reproducible and accurate histopathologic diagnoses. Results of simulated consultation are shown in Figure 5. We found near-perfect concordance between SRH and H&E histology for diagnosing nonlesional and lesional tissue ($\kappa = 0.86$ – 1.00), as well as

low-grade and high-grade pediatric brain tumors ($\kappa = 0.86$ – 1.00). Diagnostic accuracy for the above metrics (survey SRH/H&E diagnosis vs. final diagnosis) was greater than 92% for both SRH and H&E histology. For predicting the histopathologic class, there was also near-perfect concordance ($\kappa = 0.90$ – 0.95) and high

**Figure 3.**

SRH identifies pediatric surgical lesions of the posterior fossa. Magnetic resonance images (midsagittal T1-weighted post-gadolinium) of the three most common surgical lesions of posterior fossa are shown: pilocytic astrocytoma (**A**), ependymoma (**E**), and medulloblastoma (**I**). Pilocytic astrocytoma SRH shows biphasic pattern (black dashed line; **B**) with protein-rich pilocytic processes (**C**) and Rosenthal fibers (**D**). Ependymomas demonstrate rosette formation (**F**) and pseudorosette formation shown in cross-section (**G**) and longitudinal section (**H**). Medulloblastomas are densely hypercellular on low- (**J**) and high-magnification (**K**). Homer-Wright rosette formation (**L**) is visualized throughout the SRH mosaic. Scale bars, 100 μ m in large tiles; 50 μ m in small tiles.

accuracy for both modalities (SRH, 92–96%; H&E 92–100%). These results indicate that pathologists' ability to determine histopathologic diagnoses of fresh pediatric brain tumor specimens using SRH images is highly concordant and as accurate as current standard of care methods.

Image feature extraction and quantitative histology using SRH

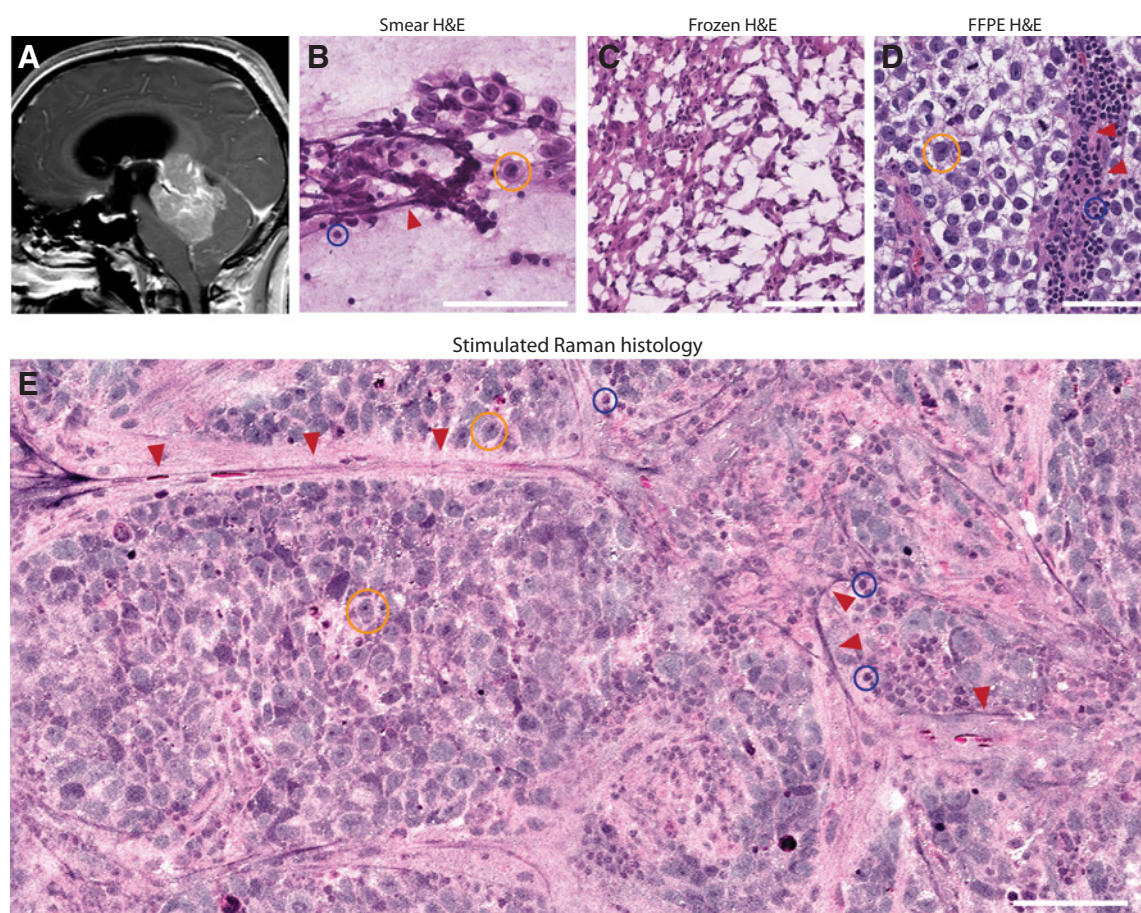
The supervising neuropathologist (A.P. Lieberman) selected 30 SRH images for quantitative histologic analysis and image feature extraction that best represented the histologic features of normal brain and pediatric tumor tissue. Selected specimens included normal brain tissue (294 FOVs, six mosaics) and low-grade (874 FOVs, 15 mosaics) and high-grade (683 FOVs, 10 mosaics) tumors. SRH feature extraction pipeline schematic can be found in Fig. 6. A statistically significant difference ($P < 0.001$) in nuclear density was identified for normal tissue (11.7 ± 10.9 cells), low-grade tumors (123.4 ± 88.4 cells), and high-grade tumors (422.9 ± 268.3 ; Fig. 6). A significant difference ($P < 0.001$) was also identified in TAM density between normal (0.0 ± 0.0 cells), low-grade (2.8 ± 6.0 cells), and high-grade (11.4 ± 14.8 cells; Fig. 6). A weak, but statistically significant ($P < 0.001$), correlation was identified between nuclear density and TAM

density, with a correlation coefficient of 0.18 (95% confidence interval, 0.12–0.21; Fig. 6).

Nuclear morphology parameters with the greatest normalized difference between groups (i.e., normal vs. low-grade vs. high-grade) were area, perimeter, eccentricity, and maximum feret diameter. Box plots of these parameters can be found in Fig. 6. With increased degree of malignancy, a trend towards increased nuclear size was found (i.e. greater nuclear/cytoplasmic ratio with tumor anaplasia). As shown in Fig. 6 box plots, median normal nuclei area was 304 pixels, compared to 314 pixels for low-grade tumors and 370 for high-grade tumors ($P < 0.001$). A similar upward trend was found for median perimeter (normal = 94 pixels, low-grade = 109 pixels, high-grade = 113 pixels, $P < 0.001$) and maximum feret diameter (normal = 27.9 pixels, low-grade = 30.5 pixels, high-grade = 32.0 pixels, $P < 0.001$).

Machine-learning-based classification of fresh pediatric brain specimens

To develop a supervised machine-learning method that utilizes the SRH image features described above, we trained and implemented a random forest model for rapid, automated intraoperative classification of fresh tissue specimens. Nuclear density, TAM

**Figure 4.**

SRH preserves cytologic and histoarchitectural features of pediatric brain tumors. **A**, Preoperative midsagittal T1-weighted post-gadolinium magnetic resonance image of posterior fossa germinoma. **B**, Smear preparation shows the large germ cells with abundant foamy glycogen-rich cytoplasm (yellow circle), admixed with reactive small lymphocyte (blue circle) adjacent to blood vessels (red arrows). **C**, Frozen sectioning causes freezing artifact that disrupts essential cytologic features of germinoma, severely limiting interpretation. **D**, Formalin-fixed, paraffin-embedded (FFPE) H&E section shows large tumor cells with prominent nucleoli and mature lymphocytes adjacent to blood vessels (red arrows). **E**, Similar to FFPE image, key diagnostic features are shown in SRH with preserved specimen cytology and histoarchitecture, allowing for unhindered interpretation and accurate histopathologic diagnosis.

density, and nuclear morphology parameters were used as model predictors. Evaluating the ability of our random forest model 1 to predict normal versus lesional tissue at the SRH FOV level, we achieved $93.8 \pm 2.2\%$ accuracy on cross-validation (optimized mtry hyperparameter = 7). ROC analysis of random forest classifier values found an AUC of .970 (Fig. 7). For predicting low-grade tissue versus high-grade tissue, we achieved an accuracy of $89.4 \pm 1.9\%$ (optimized mtry hyperparameter = 2) with AUC of 0.96 (Fig. 7). Extracted image features with highest importance as measured by mean Gini impurity decrease were nuclear density, TAM density, nuclear compactness, and maximum radius. For a full listing of model variable importance, see Supplementary Figs. S1 and S2.

Mosaic-level, or specimen-level, classification was achieved by assigning the most common FOV class within a mosaic, as determined by random forest predictions, to the entire mosaic. As an illustrative example, a ganglioglioma, WHO grade I, is shown in Fig. 7. Model 1 predicted 23/49 FOVs as nonlesional (47%) and the remaining 26/49 (53%) FOVs as lesional. The mosaic is, therefore, correctly classified as lesional because greater

than 50% of FOVs were correctly predicted. Model 2 identified an abundance of low-grade histopathology [47/49 FOVs (96%)], consistent with a WHO grade I lesion. Fig. 7 shows each of the 25 mosaics included for analysis and the corresponding random forest predictions represented as percentage of FOV tiles. Using our modal approach for classifying SRH image mosaics, we achieved 100% accuracy for classifying lesional and nonlesional specimens and classifying low-grade and high-grade tumors.

Discussion

Rapid, accurate histopathologic diagnosis is essential for providing optimal surgical care in pediatric brain tumor patients. We demonstrate that SRH is a viable alternative to conventional histology for providing intraoperative histology without the need for tissue processing, sectioning, or staining. SRH was able to highlight the diagnostic features of common pediatric type brain tumors. Near-perfect diagnostic concordance and accuracy indicates a similar degree of diagnostic yield contained within SRH and CH images. In addition to providing diagnostic quality

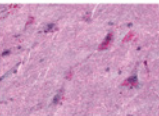
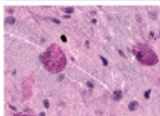
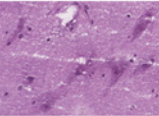
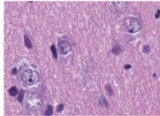
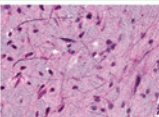
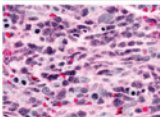
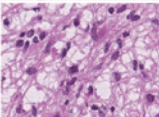
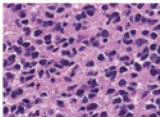
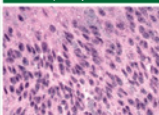
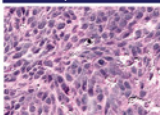
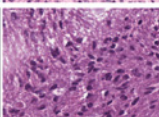
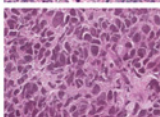
		Specimen type	Imaging modality	Neuropathologist 1		Neuropathologist 2		Neuropathologist 3		Interrater		
				Correct	Incorrect	Correct	Incorrect	Correct	Incorrect	accuracy		
A	Nonlesional: Normal cortex		Lesional: Ganglioglioma		Diagnosing nonlesional and lesional specimens							
	SRH			Normal specimens	H&E	4	1	5	0	5	0	93.3
					SRH	4	1	5	0	5	0	93.3
				Low-grade tumors	H&E	12	1	13	0	13	0	97.4
					SRH	13	0	13	0	12	1	97.4
	H&E			High-grade tumors	H&E	7	0	7	0	7	0	100
					SRH	7	0	7	0	7	0	100
				Total	H&E	23	2	25	0	25	0	97.3
					SRH	24	1	25	0	24	1	97.3
	Intrater accuracy				H&E	92	100	100				
				SRH	96	100	96					
Concordance (κ)				0.86		1		0.88				
B	Low-grade tumor: Pilocytic astrocytoma		High-grade tumor: Medulloblastoma		Diagnosing low-grade and high-grade tumors							
	SRH			Low-grade tumors	H&E	12	0	13	0	13	0	100
					SRH	12	0	13	0	13	0	100
				High-grade tumors	H&E	7	0	7	0	7	0	100
					SRH	7	0	6	1	7	0	100
	H&E			Total	H&E	20	0	20	0	20	0	100
					SRH	20	0	19	1	20	0	98.3
				Intrater accuracy		H&E	100	100	100			
						SRH	100	95	100			
	Concordance (κ)				1		0.86		1			
C	Survey diagnosis: Ependymoma		Survey diagnosis: Embryonal tumor		Diagnosing histopathologic class							
	SRH			Normal specimens	H&E	4	1	5	0	5	0	93.3
					SRH	4	1	5	0	5	0	93.3
				Low-grade tumors	H&E	11	1	13	0	13	0	94.8
					SRH	12	0	12	1	12	1	92.3
	H&E			High-grade tumors	H&E	7	0	7	0	7	0	100
					SRH	7	0	6	1	6	1	90.4
				Total	H&E	23	2	25	0	25	0	97.3
					SRH	24	1	23	2	23	2	93.3
	Intrater accuracy				H&E	92	100	100				
				SRH	96	92	92					
Concordance (κ)				0.95		0.91		0.9				

Figure 5.

Evaluation of SRH via simulated intraoperative pathology consultation. Results from web-based survey shown in the table. SRH and standard H&E images from 25 patients were presented to three neuropathologists for evaluation. Free-text responses were evaluated on three levels: (i) normal vs. lesional (**A**), (ii) low-grade vs. high-grade (**B**), and (iii) histopathologic diagnosis (**C**). Examples of images included in the survey are shown with corresponding SRH and H&E images above: normal cortex; ganglioglioma, WHO grade I; pilocytic astrocytoma, WHO grade I; medulloblastoma, WHO grade IV; ependymoma, WHO grade II; and embryonal tumor other than medulloblastoma, WHO grade IV.

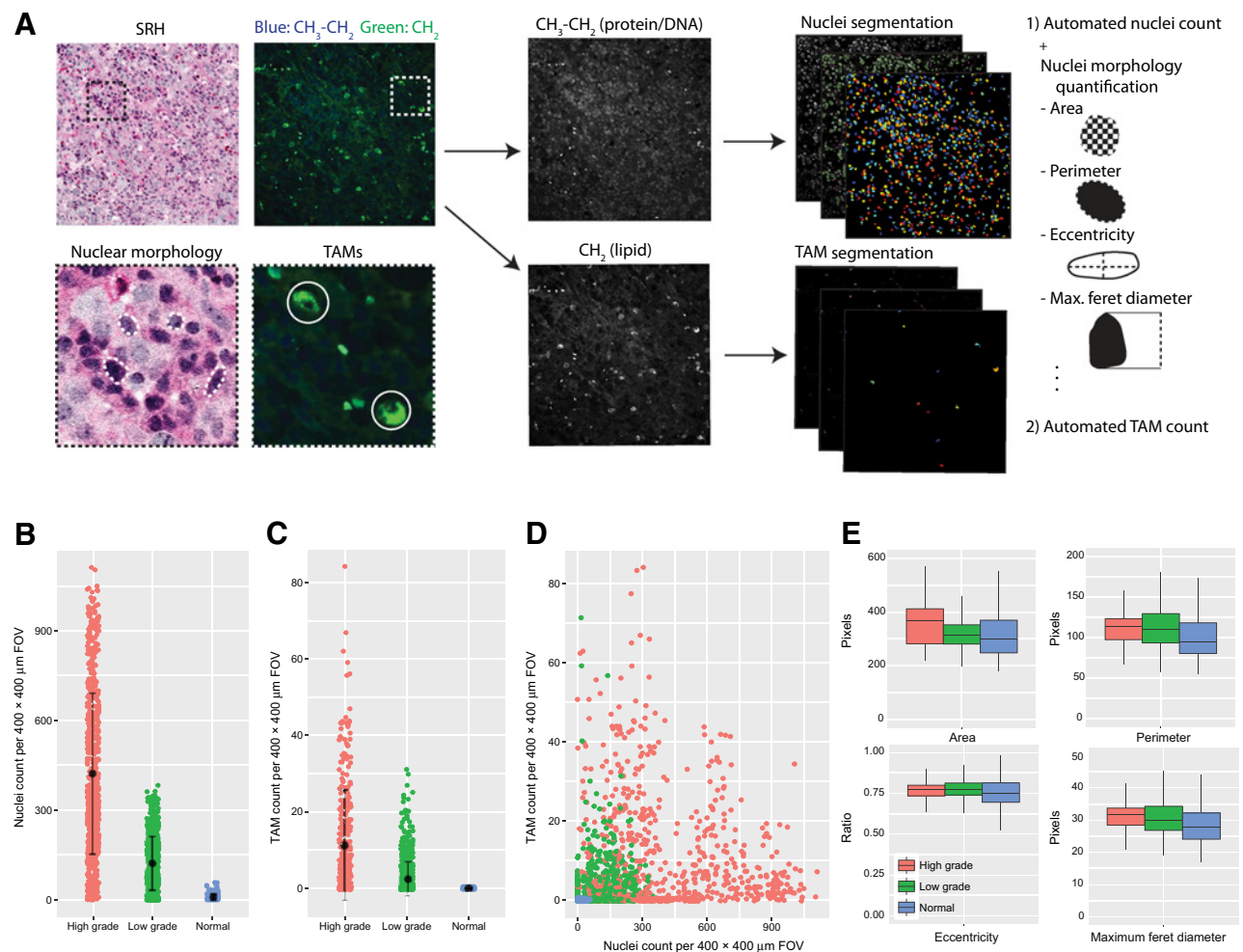
images, SRH also allows for rapid quantitative histology through digital image processing. By leveraging the image contrast contained in the $2,845\text{ cm}^{-1}$ (CH_2/lipid) and $2,930\text{ cm}^{-1}$ ($\text{CH}_3/\text{protein}$) channels, we were able to identify and segment TAMs and tumor nuclei for feature extraction and quantitative image analysis. Using cellularity and nuclear morphologic parameters, random forest machine-learning models accurately identified lesional tissue and tumor grade at both the FOV level and specimen level for automated classification of pediatric brain tumor specimens.

Sampling high-quality, lesional tissue within a resection cavity is paramount for establishing a final pathologic diagnosis using conventional histology and molecular markers. The increasing importance of molecular diagnostics in pediatric neuro-oncology, including *WNT*-activation, *Shh*-activation, *BRAF* mutations, *RELA* fusion, and *H3 K27M*-mutation, among others, requires a standardized and streamlined intraoperative histology system that ensures high diagnostic yield from sampled tissue (14). SRH, as a label-free and non-destructive optical imaging modality, allows for the same tissue to be imaged intraoperatively and subsequently used for permanent fixation and molecular testing (10, 11, 19).

This advantage of SRH over conventional histology is especially important when only scant tissue can be safely sampled due to tumor location in eloquent brain regions, such as with diffuse midline gliomas. Because SRH requires only minimal tissue for intraoperative diagnosis and the same specimen can be used for final diagnosis, SRH is well positioned to impact the practice of both histopathologic and molecular diagnoses of pediatric brain tumors.

Although other optical imaging modalities, including fluorescence-guided surgery with 5-aminolevulinic acid (20), coherent anti-Stokes Raman scattering microscopy (21, 22), Raman spectroscopy (23, 24), mass spectrometry (25–27), optical coherent tomography (2), and confocal microscopy (3, 4), have been used to detect brain tumor infiltration, SRH provides diagnostic quality images that allow for histopathologic assessment of tissue that compares with standard H&E histology. Because SRH images are acquired digitally, they can be immediately uploaded to a health system's picture archiving and communications (PACS) system, as is done in our own medical center. PACS-based SRH provides an opportunity for remote neuropathology assessment of intraoperative images and integration of SRH images into stereotactic

Hollon et al.

**Figure 6.**

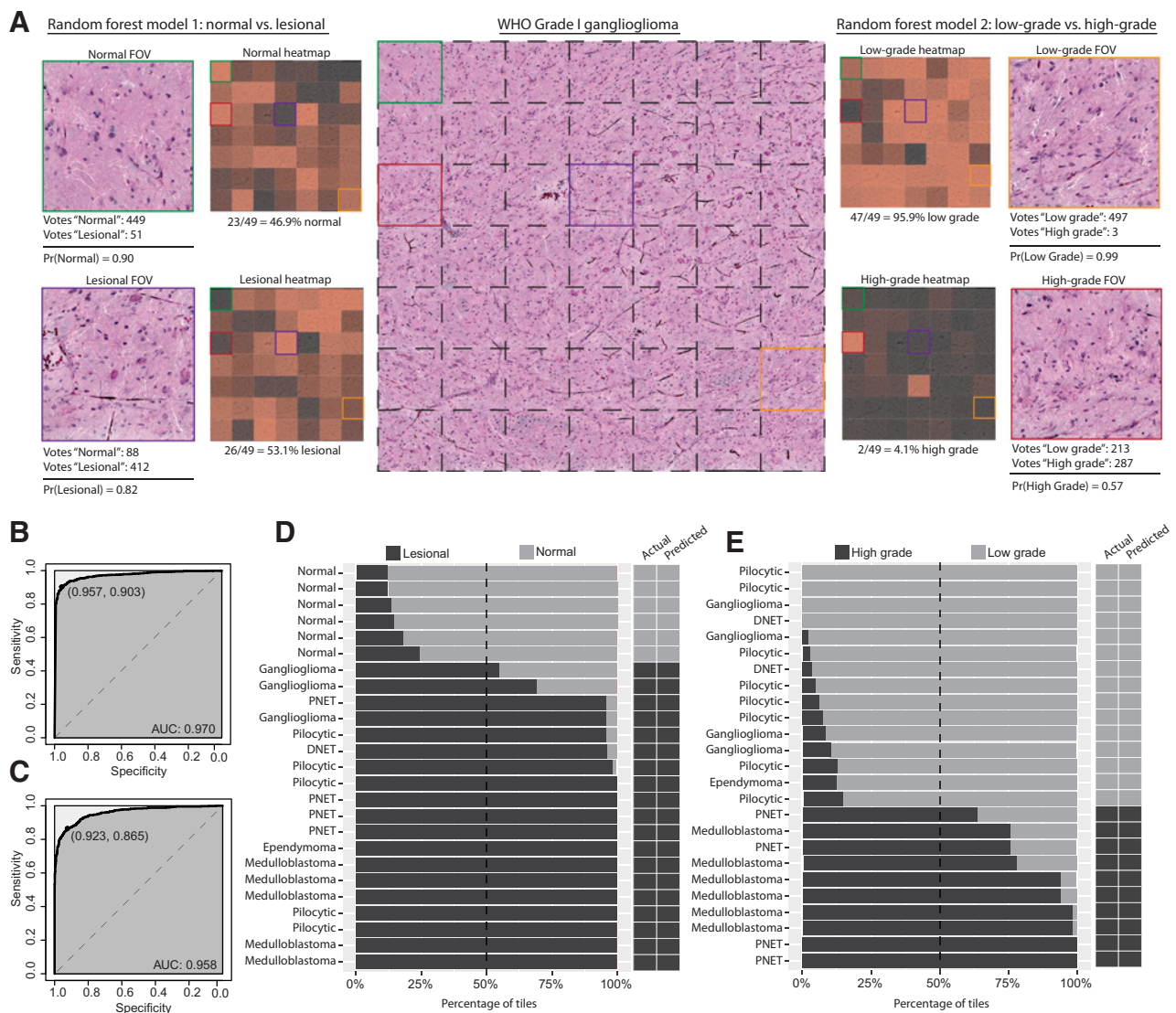
SRH feature extraction and quantitative histology. **A**, CellProfiler feature extraction pipeline was developed to split composite SRH images into 2845 cm¹/CH₂ and 2,930–2,845 cm¹/CH₃-CH₂ images for nuclear and TAM segmentation, respectively. Automated cell counting was implemented for each FOV. Morphologic analysis was then completed for each segmented nuclei as a measure of nuclear anaplasia. Automated nuclear (**B**) and TAM (**C**) counts are associated with increasing tumor grade and show a weak linear correlation (**D**). **E**, Nuclear morphology parameters show statistically significant trend towards larger nuclei with increasing tumor grade.

navigational systems. Registered neurosurgical instruments can assign spatial coordinates to the location of the specimen biopsy; histologic features from SRH images can then be represented in a three-dimensional tumor cavity. SRH combined with stereotactic navigational systems has the potential to guide tumor removal, improve safe maximal resection, and improve patient outcomes.

SRH provides a novel histologic dataset that allows for quantitative histology and intraoperative computer-aided diagnosis (CAD). Machine-learning algorithms for diagnostic classification have been applied to multiple imaging modalities across disciplines, including brain tumors (28–30), diabetic retinopathy (31), dermatologic lesions (32), lung cancer (33), and breast lesions (34, 35). CAD can ultimately reduce inter-rater variability and standardize intraoperative pathology. In addition, intraoperative SRH-based CAD can reduce operative time by (i) eliminating the need for tissue processing and (ii) decreasing the time for image interpretation.

Our previous work using SRH for machine-learning-based diagnosis was a proof-of-concept for applying high-level pattern recognition techniques combined with a multilayer perceptron for tumor classification (13). The aim of the current study was to extract specific and known histopathologic features of neoplastic tissues and deploy a machine-learning algorithm to map specific image features to pediatric brain tumor diagnoses. Random forest models are amenable to determining the importance of each image feature for brain tumor classification. By extracting specific image features and using a highly interpretable machine-learning method, we determine that known histopathologic features used by the neuropathologist to identify lesional tissue and diagnosis tumor grade can also be used for machine-learning-based pediatric brain tumor diagnosis.

Our random forest classifier was able to accurately identify lesional tissue, which can improve the diagnostic yield of collected specimens and guide tumor resection via rapid, automated

**Figure 7.**

Validation of machine-learning model for classification of pediatric brain tumor specimens. **A**, SRH image mosaic (center) of a ganglioglioma, WHO grade I, is shown with individual FOV tiles demarcated with dashed black lines. Select color-coded tiles from the image mosaic are shown peripherally to demonstrate the random forest classifier. Model 1 (left) classified the green-labeled FOV as normal with 90% probability, receiving 449/500 tree votes. By contrast, purple labeled FOV was classified as lesional with 82% probability, receiving 412/500 tree votes. Normal and lesional classifier probabilities are shown for each mosaic FOV in adjacent heatmap. Mosaic is correctly classified as lesional with 53.1% (i.e., modal class) of tiles voted lesional. Model 2 (right) follows similar implementation; the majority of tiles are classified as low-grade with high probability. **B**, ROC analysis for FOV-level performance of model 1. Optimized sensitivity and specificity are shown. **C**, ROC analysis for FOV-level performance of model 2. **D**, Model 1 mosaic-level performance shown as cumulative percentage of tiles with normal or lesional classification within each mosaic. Dashed line represents the threshold for modal diagnosis and results are shown in adjacent columns. **E**, Model 2 mosaic-level performance for differentiating low-grade and high-grade tumors (DNET, dysembryoplastic neuroepithelial tumor).

classification of specimens. Extent of resection is a major modifiable risk factor for improved clinical outcomes in pediatric brain tumors. Evidence supports that gross-total or near-total resection confers longer progression-free and overall survival in patients with ependymomas and pilocytic astrocytomas (5–8). Conversely, aggressive surgical resection has not been shown to be of benefit in medulloblastoma (9). The divergence of surgical goals depending on intraoperative diagnosis of tumor grade makes accurate detection of low-grade versus high-grade features within tumor resection cavities essential both for surgical management and providing optimal adjuvant treatments in the postoperative

setting. SRH-based CAD provides a streamlined and accurate system for serial biopsies throughout a brain tumor resection to better characterize tumor heterogeneity, inform surgical goals and improve extent of resection.

Future directions for using SRH as a system for intraoperative pediatric brain pathology include validating SRH in a large, multi-institutional cohort of pediatric patients. Validating SRH in a larger cohort will allow for a more nuanced diagnosis of rare brain tumors and better analysis of its performance across multiple brain tumor types. Machine-learning classification of tumor specimens into WHO diagnoses was not possible due to sample size

Hollon et al.

limitations, however larger image datasets will make this plausible in the near future. With larger SRH datasets, deep learning and convolutional neural networks may be used for robust, automated feature extraction that can improve accuracy of pediatric brain tumor diagnosis. Finally, the integration of SRH imaging data with clinical, molecular, and genomic patient information may improve diagnostic classification and provide more personalized treatment options for pediatric brain tumor patients.

Disclosure of Potential Conflicts of Interest

D.A. Orringer has ownership interest (including patents) in Invenio Imaging Inc., and is a consultant/advisory board member for Invenio Imaging Inc. No potential conflicts of interest were disclosed by the other authors.

Authors' Contributions

Conception and design: T.C. Hollon, S. Lewis, B. Pandian, K. Muraszko, S. Camelo-Piragua, D.A. Orringer

Development of methodology: T.C. Hollon, S. Lewis, B. Pandian, S. Camelo-Piragua, D.A. Orringer

Acquisition of data (provided animals, acquired and managed patients, provided facilities, etc.): T.C. Hollon, B. Pandian, M.R. Garrard, H. Garton, C.O. Maher, K. McFadden, A.P. Lieberman, K. Muraszko, S. Camelo-Piragua, D.A. Orringer

Analysis and interpretation of data (e.g., statistical analysis, biostatistics, computational analysis): T.C. Hollon, S. Lewis, B. Pandian, Y.S. Niknafs, M. Snuderl, K. Muraszko, S. Camelo-Piragua, D.A. Orringer

Writing, review, and/or revision of the manuscript: T.C. Hollon, S. Lewis, B. Pandian, Y.S. Niknafs, H. Garton, K. McFadden, M. Snuderl, K. Muraszko, S. Camelo-Piragua, D.A. Orringer

Administrative, technical, or material support (i.e., reporting or organizing data, constructing databases): T.C. Hollon, B. Pandian, M.R. Garrard, K. Muraszko, D.A. Orringer

Study supervision: K. Muraszko, S. Camelo-Piragua, D.A. Orringer

Acknowledgments

D.A. Orringer received grant support from the following: National Institute of Biomedical Imaging and Bioengineering (R01EB017254), National Cancer Institute of the NIH (P30CA046592), Fast Forward Medical Innovation, U-M Michigan Translational Research and Commercialization for Life Sciences Program (U-M MTRAC), and Michigan Institute for Clinical and Health Research (2UL1TR000433).

The costs of publication of this article were defrayed in part by the payment of page charges. This article must therefore be hereby marked *advertisement* in accordance with 18 U.S.C. Section 1734 solely to indicate this fact.

Received July 10, 2017; revised September 5, 2017; accepted October 26, 2017; published OnlineFirst November 1, 2017.

References

- Somerset HL, Kleinschmidt-DeMasters BK. Approach to the intraoperative consultation for neurosurgical specimens. *Adv Anat Pathol* 2011;18:446–9.
- Kut C, Chaichana KL, Xi J, Raza SM, Ye X, McVeigh ER, et al. Detection of human brain cancer infiltration ex vivo and in vivo using quantitative optical coherence tomography. *Sci Transl Med* 2015;7:292ra100.
- Sanai N, Eschbacher J, Hattendorf G, Coons SW, Preul MC, Smith KA, et al. Intraoperative confocal microscopy for brain tumors: a feasibility analysis in humans. *Neurosurgery* 2011;68:282–90; discussion 90.
- Sanai N, Snyder LA, Honea NJ, Coons SW, Eschbacher JM, Smith KA, et al. Intraoperative confocal microscopy in the visualization of 5-aminolevulinic acid fluorescence in low-grade gliomas. *J Neurosurg* 2011;115:740–8.
- Bandopadhyay P, Berghthold G, London WB, Goumnerova LC, Morales La Madrid A, Marcus KJ, et al. Long-term outcome of 4,040 children diagnosed with pediatric low-grade gliomas: an analysis of the Surveillance Epidemiology and End Results (SEER) database. *Pediatr Blood Cancer* 2014;61:1173–9.
- Fernandez C, Figarella-Branger D, Girard N, Bouvier-Labit C, Gouvernet J, Paz Paredes A, et al. Pilocytic astrocytomas in children: prognostic factors—a retrospective study of 80 cases. *Neurosurgery* 2003;53:544–53; discussion 54–5.
- Grill J, Le Deley MC, Gambarelli D, Raquin MA, Couanet D, Pierre-Kahn A, et al. Postoperative chemotherapy without irradiation for ependymoma in children under 5 years of age: a multicenter trial of the French Society of Pediatric Oncology. *J Clin Oncol* 2001;19:1288–96.
- Merchant TE, Li C, Xiong X, Kun LE, Boop FA, Sanford RA. Conformal radiotherapy after surgery for paediatric ependymoma: a prospective study. *Lancet Oncol* 2009;10:258–66.
- Thompson EM, Hielscher T, Bouffet E, Remke M, Luu B, Gururangan S, et al. Prognostic value of medulloblastoma extent of resection after accounting for molecular subgroup: a retrospective integrated clinical and molecular analysis. *Lancet Oncol* 2016;17:484–95.
- Freudiger CW, Min W, Saar BG, Lu S, Holtom GR, He C, et al. Label-free biomedical imaging with high sensitivity by stimulated Raman scattering microscopy. *Science* 2008;322:1857–61.
- Ji M, Orringer DA, Freudiger CW, Ramkissoon S, Liu X, Lau D, et al. Rapid, label-free detection of brain tumors with stimulated Raman scattering microscopy. *Sci Transl Med* 2013;5:201ra119.
- Ji M, Lewis S, Camelo-Piragua S, Ramkissoon SH, Snuderl M, Venneti S, et al. Detection of human brain tumor infiltration with quantitative stimulated Raman scattering microscopy. *Sci Transl Med* 2015;7:309ra163.
- Orringer DA, Pandian B, Niknafs YS, Hollon TC, Boyle J, Lewis S, et al. Rapid intraoperative histology of unprocessed surgical specimens via fibre-laser-based stimulated Raman scattering microscopy. *Nat Biomed Eng* 2017;1:Article 0027. doi: 10.1038/s41551-016-0027.
- Louis DN, Perry A, Reifenberger G, von Deimling A, Figarella-Branger D, Cavenee WK, et al. The 2016 world health organization classification of tumors of the central nervous system: a summary. *Acta Neuropathol* 2016;131:803–20.
- Carpenter AE, Jones TR, Lamprecht MR, Clarke C, Kang IH, Friman O, et al. CellProfiler: image analysis software for identifying and quantifying cell phenotypes. *Genome Biol* 2006;7:R100.
- Breiman L. Random forests. *Machine Learning* 2001;45:5–32.
- Cohen J. A coefficient of agreement for nominal scales. *Educ Psychol Meas* 1960;20:37–46.
- Fleiss JL, Cohen J. The equivalence of weighted kappa and the intraclass correlation coefficient as measures of reliability. *Educ Psychol Meas* 1973;33:613–9.
- Lu FK, Calligaris D, Olubiyi OI, Norton I, Yang W, Santagata S, et al. Label-free neurosurgical pathology with stimulated Raman imaging. *Cancer Res* 2016;76:3451–62.
- Stummer W, Pichlmeier U, Meinel T, Wiestler OD, Zanella F, Reulen HJ, et al. Fluorescence-guided surgery with 5-aminolevulinic acid for resection of malignant glioma: a randomised controlled multicentre phase III trial. *Lancet Oncol* 2006;7:392–401.
- Camp CH, Jr., Lee YJ, Heddleston JM, Hartshorn CM, Hight Walker AR, Rich JN, et al. High-speed coherent Raman fingerprint imaging of biological tissues. *Nat Photonics* 2014;8:627–34.
- Evans CL, Xu X, Kesari S, Xie XS, Wong ST, Young GS. Chemically-selective imaging of brain structures with CARS microscopy. *Opt Express* 2007;15:12076–87.
- Jermyn M, Mok K, Mercier J, Desroches J, Pichette J, Saint-Arnaud K, et al. Intraoperative brain cancer detection with Raman spectroscopy in humans. *Sci Transl Med* 2015;7:274ra19.
- Hollon T, Lewis S, Freudiger CW, Sunney Xie X, Orringer DA. Improving the accuracy of brain tumor surgery via Raman-based technology. *Neurosurg Focus* 2016;40:E9.
- Santagata S, Eberlin LS, Norton I, Calligaris D, Feldman DR, Ide JL, et al. Intraoperative mass spectrometry mapping of an onco-metabolite to guide brain tumor surgery. *Proc Natl Acad Sci U S A* 2014;111:11121–6.

26. Eberlin LS, Norton I, Orringer D, Dunn IF, Liu X, Ide JL, et al. Ambient mass spectrometry for the intraoperative molecular diagnosis of human brain tumors. *Proc Natl Acad Sci U S A* 2013;110:1611–6.
27. Balog J, Sasi-Szabo L, Kinross J, Lewis MR, Muirhead LJ, Veselkov K, et al. Intraoperative tissue identification using rapid evaporative ionization mass spectrometry. *Sci Transl Med* 2013;5:194ra93.
28. Barker J, Hoogi A, Depeursinge A, Rubin DL. Automated classification of brain tumor type in whole-slide digital pathology images using local representative tiles. *Med Image Anal* 2016;30:60–71.
29. Mousavi HS, Monga V, Rao G, Rao AU. Automated discrimination of lower and higher grade gliomas based on histopathological image analysis. *J Pathol Inform* 2015;6:15. doi: 10.4103/2153-3539.153914.
30. Ertosun MG, Rubin DL. Automated grading of gliomas using deep learning in digital pathology images: a modular approach with ensemble of convolutional neural networks. *AMIA Annu Symp Proc* 2015; 2015:1899–908.
31. Gulshan V, Peng L, Coram M, Stumpe MC, Wu D, Narayanaswamy A, et al. Development and validation of a deep learning algorithm for detection of diabetic retinopathy in retinal fundus photographs. *JAMA* 2016;316: 2402–10.
32. Esteva A, Kuprel B, Novoa RA, Ko J, Swetter SM, Blau HM, et al. Dermatologist-level classification of skin cancer with deep neural networks. *Nature* 2017;542:115–8.
33. Yu KH, Zhang C, Berry GJ, Altman RB, Re C, Rubin DL, et al. Predicting non-small cell lung cancer prognosis by fully automated microscopic pathology image features. *Nat Commun* 2016;7:12474. doi: 10.1038/ncomms12474.
34. Cheng JZ, Ni D, Chou YH, Qin J, Tiu CM, Chang YC, et al. Computer-aided diagnosis with deep learning architecture: applications to breast lesions in US images and pulmonary nodules in CT scans. *Sci Rep* 2016;6:24454. doi: 10.1038/srep24454.
35. Cruz JA, Wishart DS. Applications of machine learning in cancer prediction and prognosis. *Cancer Inform* 2007;2:59–77.

Cancer Research

The Journal of Cancer Research (1916–1930) | The American Journal of Cancer (1931–1940)

Rapid Intraoperative Diagnosis of Pediatric Brain Tumors Using Stimulated Raman Histology

Todd C. Hollon, Spencer Lewis, Balaji Pandian, et al.

Cancer Res 2018;78:278-289. Published OnlineFirst November 1, 2017.

Updated version	Access the most recent version of this article at: doi: 10.1158/0008-5472.CAN-17-1974
Supplementary Material	Access the most recent supplemental material at: http://cancerres.aacrjournals.org/content/suppl/2017/11/01/0008-5472.CAN-17-1974.DC1

Cited articles	This article cites 35 articles, 10 of which you can access for free at: http://cancerres.aacrjournals.org/content/78/1/278.full#ref-list-1
-----------------------	--

E-mail alerts	Sign up to receive free email-alerts related to this article or journal.
Reprints and Subscriptions	To order reprints of this article or to subscribe to the journal, contact the AACR Publications Department at pubs@aacr.org .
Permissions	To request permission to re-use all or part of this article, use this link http://cancerres.aacrjournals.org/content/78/1/278 . Click on "Request Permissions" which will take you to the Copyright Clearance Center's (CCC) Rightslink site.